# **Programming Fluid Motion Using Multi-Enzyme Micropump Systems**

Jiaqi Song,<sup>1</sup> Jianhua Zhang,\*<sup>2</sup>Jinwei Lin,<sup>3</sup> Oleg E. Shklyaev,<sup>4</sup> Shanid Shrestha,<sup>1</sup> Aditya Sapre,<sup>5</sup> Anna C.

Balazs,\*<sup>4</sup> and Ayusman Sen\*<sup>1,5</sup>

<sup>1</sup>Department of Chemistry, The Pennsylvania State University,

University Park, Pennsylvania 16802, USA

<sup>2</sup>College of Chemistry and Chemical Engineering, Wuhan Textile University,

Wuhan 430200, China

<sup>3</sup>International School of Materials Science and Engineering, Wuhan University of Technology, Wuhan 430070, China

<sup>4</sup>Department of Chemical Engineering, University of Pittsburgh,

Pittsburgh, Pennsylvania 15260, USA

<sup>5</sup>Department of Chemical Engineering, The Pennsylvania State University,

University Park, Pennsylvania 16802, USA

\*Email: jhzhang@wtu.edu.cn; balazs@pitt.edu; asen@psu.edu

#### **Abstract**

In the presence of appropriate substrates, surface-anchored enzymes can act as pumps and propel fluid through microchambers. Understanding the dynamic interplay between catalytic reactions and fluid flow is vital to enhancing the accuracy and utility of flow technology. Through

a combination of experimental observations and numerical modelling, we show that coupled

enzyme pumps can exhibit flow enhancement, flow suppression, and changes in the

directionality (reversal) of the fluid motion. The pumps' ability to regulate the flow path is due to

the reaction selectivity of the enzymes; the resultant fluid motion is only triggered by the

presence of certain reactants. Hence, the reactants and the sequence in which they are present

in the solution, and the layout of the enzyme-attached patches form an "instruction set" that

guides the flowing solution to specific sites in the system. Such systems can operate as sensors

that indicate concentrations of reactants through measurement of the trajectory along which the

flow demonstrates maximal speed. The performed simulations suggest that the solutal

buoyancy mechanism causes fluid motion and is responsible for all the observed effects. More

broadly, our studies provide a new route for forming self-organizing flow systems that can yield

fundamental insight into non-equilibrium, dynamical systems.

Keywords: Enzyme Pumps • Buoyancy-Driven Convection • Fluid Flow • Sensor • Catalysis

2

#### 1. Introduction

In living systems, enzymes are able to convert the chemical energy released from nutrients into mechanical force, which can direct the vectorial flow of fluids and thus instigate a range of mechanical activities, including transport. 1-6 In synthetic fluidic chambers, enzymes perform an analogous form of chemo-mechanical transduction; the enzymatic reactions generate forces that spontaneously propel the flow of fluids confined in the chambers.<sup>7-9</sup> Here, we show that multiple enzyme patches (i.e., the pumps), localized on a surface, communicate with each other; depending on the nature of the enzymes and arrangement of the patches; the system autonomously steers the fluid flow along a specific pathway. The pumps' ability to regulate the flow path is due to the reaction selectivity of the enzymes; the resultant fluid motion is only triggered by the presence of certain reactants. Hence, the reactants and the sequence in which they are added to the solution and the layout of the patches form an "instruction set" that guides the flowing chemical solution to specific sites in the system. This chemically directed motion provides a new approach to control the self-assembly of immersed micro-scale objects.<sup>4,10</sup> The system also acts as a sensor, indicating the presence and quantity of a specific reactant by the generated fluid flow. 10-12 Other enzyme-based micropump sensors have been fabricated recently. 13-16

Distinct from prior studies on chemical pumps, we now demonstrate the assembly of multiple, distinct pumps into an interconnected active chemo-fluidic network in a microfluidic system. The multi-pump platform exploits specific connections (expressed in terms of chemistry and the produced vectorial flows) between separate pumps and thereby enables functionalities that cannot be realized within a single pump design. In particular, each pump in the network triggers a specific reaction to generate a particular product (output). This output serves as the input to the next pump in the network. The benefit of this design is that the system itself can perform multi-step chemical processes, allowing the entire "micro-reactor" to operate autonomously.

However, the chemistry and the resulting fluid flow pattern are intimately connected; they are not independent variables. The flow produced at one pump will affect the flow generated at a neighboring pump and hence the reaction kinetics at that pump.<sup>17</sup> Hence, information about the system's spatiotemporal behavior must also be taken into account in the design process.

In the studies described here, we determine how the coupling of the pumps in a network controls the rates of chemical reactions and generates fluidic patterns that can be harnessed to perform specific functions (for example, characterize the chemical composition of solution by the directionality of produced flows). The results help formulate guidelines that can be applied to larger, more extensive systems to facilitate the design of autonomous fluidic micro-reactors and devices with a wide range of functionalities.

In the cases considered below, the fluid flow is triggered by the solutal buoyancy mechanism. If the molecular volume of the reactants and the products of the reaction are different, then the system will generate local density gradients, which give rise to forces that induce fluid motion in the system.<sup>18–20</sup> If the products are denser (occupy less volume) than the reactants and the enzyme-attached patch is located on the top wall of the fluid-filled chamber, then the dense, product-laden fluid at the patch initially moves downward and forms convective rolls that circulate towards the patch on the top (as indicated by the direction of the arrows in **Figure 1C**). This motion constitutes inward pumping. Conversely, when the products are less dense than the reactants, the fluid circulates in the opposite direction, flowing away from the patch at the top and constitutes outward pumping (as indicated by the direction of the arrows in **Figure 1D**). The convective fluid flow performs useful mechanical work as it transports molecules and particles, and changes the shape of immersed, flexible materials.<sup>21–23</sup> Thus far, the reported enzyme pumps have involved at most two enzymes, limiting the dynamic behavior of the generated flow.<sup>24–26</sup> The use of multi-enzyme micropumps, however, would allow the design

and spatiotemporal control of more complex flow patterns, which can introduce new functionality and enhance the utility of fluidic devices.

The specific enzymes used here involve urease, catalase, alkaline phosphatase (AkP), and glucose oxidase (GOx) (**Figure 1**). Depending on the enzymes employed and the distance between the patches, we observe the enhancement or cancellation of fluidic flow. Controllable long-range, time-dependent fluid flow reversal was also demonstrated using enzyme cascades (e.g., AkP/GOx/catalase). The experimental results are in good agreement with the corresponding simulations performed in this study.

The numerous studies on the coupling of reaction and diffusion have revealed a plethora of patterns, many of which resemble biological designs, and provide significant insight into non-equilibrium behavior. In contrast, there have been few studies describing the effects of coupling reaction and convection processes. These results reveal how the reaction-convection events can be utilized to regulate the flow patterns in the solution and hence, the directed delivery of specific reactants to particular sites in the chamber. More generally, our findings provide a window into the rich dynamics that can emerge from the combined effects of reaction and convection.

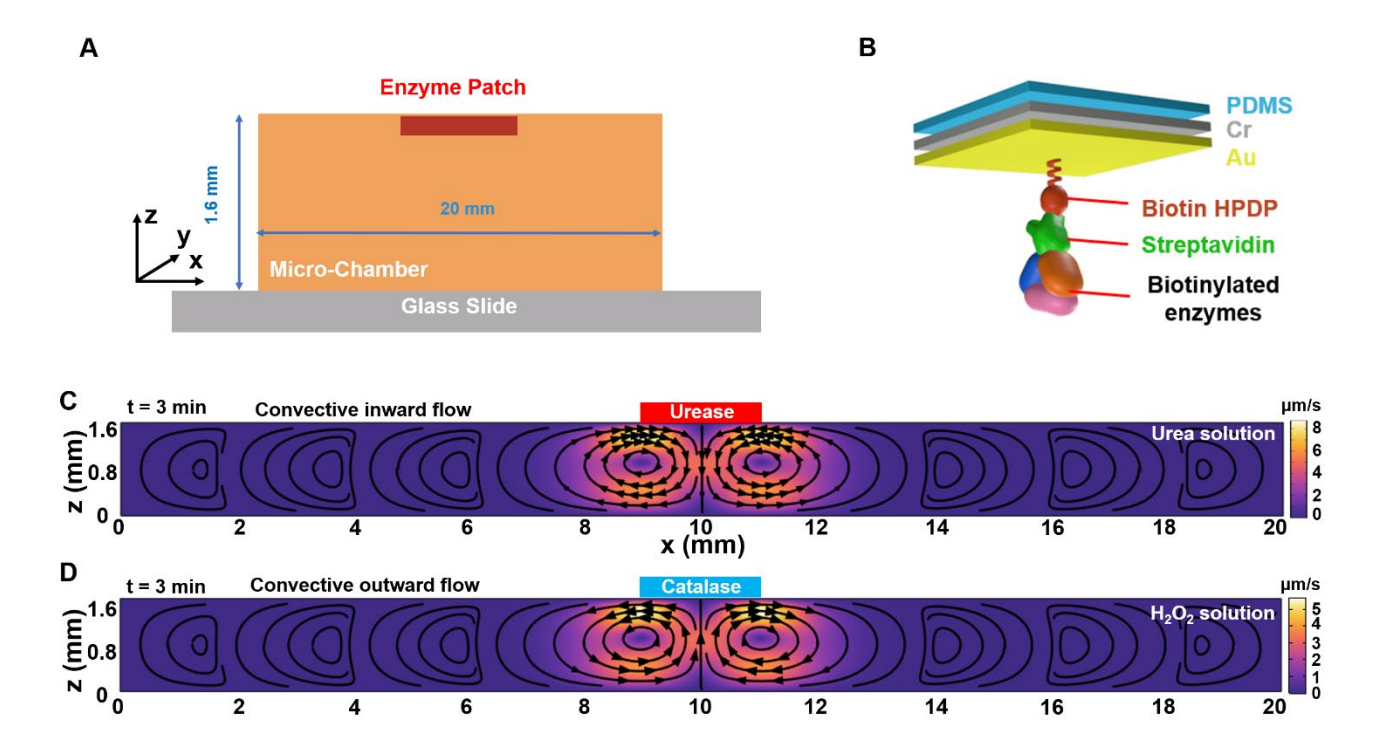


**Figure 1.** Experimental and simulative setup for the enzyme pump. (A) The illustration of the experimental setup from the side view (also see **Figure S1A**). The patch (red bar) coated by enzyme molecules was attached to the top of the chamber. (B) The layered structure of an enzyme-coated pump on a PDMS thin film. (C-D) The simulated convective flows produced by (C) a urease-coated pump and (D) a catalase-coated pump, respectively. The black arrows of the streamlines represent the flow direction, and the flow rates are quantified by the color bar.

#### 2. Experimental and Simulation Section

#### **Materials**

SYLGARD 184 silicone Elastomer (3.9 kg/ 8.6 lbs Kit) purchased from Ellsworth Adhesives, silicon wafers (diameter  $-100 \pm 0.3$  mm, Dopant - Boron, thickness  $-525 \pm 25$   $\mu$ m) obtained from Virginia Semiconductors were used for film preparations. These films were sequentially coated with 100 nm of chromium (Cr, 54 mm, VWR) and gold thin layers (Au, 57 mm, VWR).

The gold surface was biotinylated by the products generated from the reaction of EZ-Link-HPDP-Biotin (Thermal Scientific) and tributylphosphine solution (200 mM in N-methyl-2-pyrrolidinone, Sigma-Aldrich). Biotinylated enzymes were attached to the gold surface using biotin-streptavidin linkages. Specifically, EZ-Link-Sulfo-NHS-LC-LC-Biotin (Thermo Scientific) was used to anchor alkaline phosphatase and glucose oxidase to gold layer, while EZ-Link-Maleimide – PEG2 – Biotin (Thermo Scientific) and Biotin N-hydroxysuccinimide ester (Biotin-NHS, Chem Impex International) were used for respective urease and catalase attaching. The urease (Jack Bean) was obtained from TCI, while catalase (from bovine liver), AkP (bovine intestinal mucosa) and GOx (from aspergillus) were all obtained from Sigma Aldrich. Urea (Sigma Aldrich), D-glucose 6-phosphate (Sigma Aldrich), D-glucose (Sigma Aldrich), and hydrogen peroxide (30%; VWR) served as the substrates for their respective enzymes. 0.5, 2, and 3 μm polystyrene beads (Polyscience, Inc.; ~1.05 g/cm³) were dispersed in the solution to serve as tracer particles.

Preparation of dimethylpolysiloxane (PDMS) film. Sylgard-184 silicone elastomer (PDMS) and curing agent were mixed in the ratio of 10:1 with a total quantity of 5.5 g. To obtain a uniform film, a spin-coating process was performed on a silicon wafer. Initially, the wafer was spun at 200 rpm for 10 s, followed by a high-speed spin at 1000 rpm for 60 s. The film was cured at 70 °C overnight and was peeled off from the silicon wafer carefully. The film thickness was ca.120 µm. The thin PDMS film can be cut into desired shapes and sizes.

**Preparation of enzyme pumps.** A sputter coater was used to produce the Cr and Au coatings sequentially on the PDMS thin film. The metals fully covered the surface. The sputtering time was set as 60 s for both Cr and Au.

For the biotinylation of the Au surfaces, typically, 1 mg N-[6-(biotinamido) hexyl]-30-(20 pyridyldithio) propionamide (biotin HPDP) was firstly dissolved in 8 mL of dimethylformamide

(DMF), which then underwent sonication at 45 °C for 3 min. 10 μL of 200 mM tributylphosphine solution in N-methyl-2-pyrrolidinone was then added to the above solution. The reaction was incubated at 45 °C for 30 min. Next, 7 mL ethanol/water solution (ratio: 1:1) was added. The resulting solution was subsequently applied to the Au patches in a Petri dish, and it was left to incubate overnight at room temperature. The biotinylated Au surfaces were then rinsed with water and 50 mM buffer solution (HEPES for urease, catalase, AkP and GOx, pH=7.0; MES for GOx and catalase, pH=6.0). 1 mL of 2 mg/mL streptavidin buffer solution was added to the surface of Au and left incubating at room temperature for 3 h. After streptavidin attachment, the Au patterns were washed with buffer solution 3 times and dried in air.

The biotinylations of enzymes were carried out as follows. 130  $\mu$ L of 4.5 mM maleimide-PEG2-Biotin were mixed with 75 mg of urease and brought to 5 mL solution with 50 mM HEPES. Biotin-NHS in DMSO (25 mg/mL) was added into 2 mg/mL catalase solution in HEPES/MES buffer (50 mM). The final concentration of Biontin-NHS was 10 wt% of the enzyme to be biotinylated. 1136  $\mu$ L of 100  $\mu$ M Sulfo-NHS-LC-LC-biotin were added to 27 mg of alkaline phosphatase (or 9 mg of glucose oxidase) and brought to 5 mL with 50 mM buffer solution. Enzyme/biotin solutions were incubated with shaking (550 rpm) at room temperature for 2 h.

The biotinylated enzymes were centrifuged at 4500 rpm for 5 min and washed 3 times with the corresponding buffer solution in an Amicon Ultra centrifugal filter unit. The enzyme solution remaining in the filter was collected and brought to 2 mL with the buffer. 1 mL of the biotinylated-enzyme solution was added to each of the Au patterns and left incubating at room temperature for 3 h. Then, the enzyme pumps were submerged in the 50 mL buffer solution overnight in a 2-8 °C refrigerator.

**Measurement of the flow rate.** The fluid flow rate was measured in a cylindrical hybridization chamber (1.6 mm in height, 20 mm in diameter, Grace Bio-Labs) (**Figure S1A**). The enzyme

coated PDMS patches were attached to the bottom of a coverslip that was used to seal the top of the chamber (**Figure 1A, B**). 2 µm polystyrene microspheres were added as tracers to the chamber to measure the net flow velocities at different depths using a microscope (Axiovert 200 Mat; 20x magnification with a field of view of 384.8 µm x 287.1 µm). The tracers showed a velocity of  $0.05 \pm 0.2$  µm/s due to Brownian diffusion when dispersed in DI water in the absence of enzyme patches. Optical microscope was used to record the motion of the tracers at different depths of the chamber. The locations and speeds of the particles that follow the fluid flow were tracked using Tracker software, and then the trajectories of the individual tracers were plotted using Matlab. 0.5 and 3 µm polystyrene microspheres were also used with a urease pump and the observed velocities were essentially identical to that observed with 2 µm tracers. The error bars representing standard errors are obtained from 3 separate experiments and with 5 particles tracked in each experiment. All the experiments were conducted within 10 min after enzymes contacted the substrates. Unless specified, the flow velocities were measured at 75% height of the chamber. The fluid speed was defined as positive when moving toward the right, otherwise, it is negative.

Measurement of the activities of the anchored enzymes (Figure S2). The absorption spectra of the reactant and product solutions were measured using UV-Vis. The standard curve of ammonium ion concentration was measured at 500 nm by the absorbance of the iodide of Millon's base (brown product from the reaction of Nessler's reagent with ammonium ion). The standard curve of H<sub>2</sub>O<sub>2</sub> was measured at 250 nm. The increase of UV-Vis absorbance at 500 nm in urease/urea system represents the production of ammonium ions in the process; the UV-Vis absorbance decrease at 250 nm in catalase/hydrogen peroxide system represents the consumption of the reactants; while the increase at 250 nm in glucose oxidase/D-glucose represents the generation of hydrogen peroxide. 6 immobilized enzyme patches (3 mm X 3 mm in size, fully coated) were placed in a 10 mL solution with the corresponding substrates (0.1 M

urea for urease; 24 mM H<sub>2</sub>O<sub>2</sub> for catalase; 50 mM glucose for glucose oxidase). We monitored the UV-Vis absorbance change respectively for 20 min and calculated the corresponding concentrations based on the standard curves.

Numerical Simulations. To understand the fluid flow dynamics in multi-enzyme systems, we conducted numerical simulation using the diffusions and creeping flow modules of COMSOL Multiphysics software (version 6.1). To simplify the model, a two-dimensional (2D) rectangle domain was considered of length  $L_x = 20$  mm and height  $L_z = 1.6$  mm. The chamber is filled with an aqueous solution of the substrate and the immobilized enzyme patches are on the top, labeled with red or blue bars in the simulation figures. It is well-documented that, for all the concerned enzyme pumps in this work, their convective flows are caused by the solutal buoyancy mechanism. <sup>18,27</sup> The density variation induced by temperature change from the exothermic reactions was neglected here. <sup>28</sup> This solutal buoyancy mechanism results from the density difference between the reactants and the products of a reaction. Briefly, the local density difference yields a volume force acting on the fluid, thereby triggering the autonomous fluid flow. When the density of the products exceeds that of the reactants, the resulting flow is termed "inward pumping"; in the reverse case, "outward pumping" results. Due to the fluid continuity, this flow eventually recirculates in a closed space. The density variation generated by the change in the concentration  $C_i$  of reactants and products is:

$$\Delta \rho = \rho_0 \sum_{i}^{j} \beta_i C_i \tag{1}$$

Here, the i is a number denoting a reactant or product  $(1 \le i \le j)$ .  $C_i$  represent a local time-dependent concentration of the reactant i. The expansion coefficient,  $\beta_i = \frac{1}{\rho_0} \frac{\partial \rho}{\partial c_i}$ , characterizes the change in the local density of the fluid because of the presence of species i.  $\rho_0$  is the solvent density. Thus, the resulting buoyancy force per unit volume can be calculated according to  $\mathbf{F}_b = -\mathbf{g}\Delta\rho$ , where  $\mathbf{g}$  represents the gravitational acceleration.

Then, the fluid flow velocity was calculated through the Boussinesq approximation of the Navier-Stokes equation where inertia was ignored:

$$\rho \frac{\partial \mathbf{u}}{\partial t} = \nabla \cdot [-p\mathbf{I} + \mu(\nabla \mathbf{u} + (\nabla \mathbf{u})^{\mathrm{T}}] + \mathbf{F}_b$$
 (2)

and the continuity equation for the incompressible fluid,

$$\rho \nabla \cdot \mathbf{u} = 0 \tag{3}$$

where p,  $\mathbf{I}$ ,  $\mu$ , T, and  $\nabla$  are the respective pressure, unit tensor, <sup>20,29</sup> fluid dynamic viscosity, temperature, and spatial gradient operator, respectively.  $\rho$  is the real-time fluid density and  $\mathbf{u}$  is the fluid velocity. Since the gravity works in the z-direction, the force density  $\mathbf{F}_b$  has z-component only. The initial flow velocity and the pressure were all set to zero.

The time-dependent flux of reactants and products and their diffusion in solution were calculated according to the following equations:

$$\frac{\partial c_i}{\partial t} + \nabla \cdot \mathbf{J}_i + \mathbf{u} \cdot \nabla c_i = R_i \tag{4}$$

$$\mathbf{J}_i = -D_i \nabla c_i \tag{5}$$

where  $\mathbf{J}_i$  is the flux of specie i,  $D_i$  is the corresponding diffusion coefficient,  $R_i$  describes the rate of production or decomposition of chemicals during chemical reactions.

The catalytic reaction rate (r) follows the Michaelis-Menten relation:

$$r = \frac{r_{max}[C]}{K_m + [C]} \tag{6}$$

 $r_{max}$  indicates the maximum reaction rate:

$$r_{max} = nk_{cat} \cdot [E] \tag{7}$$

 $K_m$  represent the Michaelis constant of enzyme which equals to the needed substrate concentration to achieve  $1/2*r_{max}$ , [C] is the substrate concentration, n is the number of active

sites on the enzyme molecule,  $k_{cat}$  is the catalytic constant of enzyme that specifies the turnover rate per molecule, and [E] represents the enzyme concentration on the reactive surface.

Assuming that the relevant reactions occur only at the enzyme-coated surfaces (which operate as pumps) and the corresponding reactants were available in the bulk, we modeled the rates of the enzymatic reactions as

$$R_i = r \tag{8}$$

The fluid is driven by variation in the local chemical composition that is produced by the catalytic reaction around the enzyme-coated patches. Most simulations of the multi-enzyme-driven convective flows were conducted up to the time of t = 3 min, which is comparable to the time of the experimental observations.

For the arranged multiple micropump system in 2D (x-y) plane, a rectangle domain was set with a length of  $L_x$  = 20 mm and a width of  $L_y$  = 20 mm. Two square patches (2 × 2 mm²) were put in the middle of the domain, one was placed at the bottom-right corner of the other one. The parameters used for all the systems are given in the Supporting Information.

#### 3. Results and Discussion

We employed a sealed hybridization chamber (1.6 mm in height; 20 mm in diameter) filled with a solution of the corresponding substrate (**Figure 1A** and **Figure S1**). An enzyme-attached PDMS thin film was placed at the top of the chamber. As illustrated in **Figure 1B**, a functional patch (2 mm x 2 mm) on the thin film was fabricated using the covalent bonding of deposited gold to thiol (from Biotin HPDP) and the strong non-covalent interaction between biotin and streptavidin; thus, the anchored enzymes were firmly attached to the polymer film. The activities of anchored enzymes were measured (**Figure S2**). The experimental setup of the pumps was different from the previously reported enzyme pumps where the pumps were anchored at the bottom of the chamber 18,19,28; yet they share similar pumping mechanisms. When an enzymatic

reaction occurs, due to the density difference between the reactants and the products, solutal buoyancy-induced convective rolls are generated in the microchamber. For catalase, AkP and GOx, the products are less dense than the corresponding reactants and an outward pumping result. For urease, the reverse is true and thus, the system shows inward pumping. **Figure 1C** shows the simulated flow pattern (side view) at t = 3 min caused by a urease micropump. The simulation of the catalase pump is shown in **Figure 1D**. The evolution of the convective flow with time is given in **Figure S3**. The computational details are described in the Experimental Section and Supporting Information.

## Coupling "Out" and "In" Micropumps for Enhancement in Fluid Flow

The enhancement of the fluid flow is manifested as an increase in the fluid velocity produced by two combined pumps in comparison to velocities that result from each of the pumps operating separately. To demonstrate the fluid flow enhancement, we selected catalase and urease as the outward and inward pumps, respectively. The illustration in **Figure 2A** shows two square-shaped enzyme pumps (2 mm x 2 mm) placed side by side and separated by a certain distance (*D*). Polystyrene beads  $(2 \text{ }\mu\text{m})$  were suspended as tracers to record the horizontal fluid velocity by an optical microscope; the flow velocity vector in the direction from catalase to urease (from left to the right) is defined as positive. **Figure 2B** shows the motion trajectories of four tracers with both substrates (top view), while the color indicates the positive direction of motion.

The fluid flows were investigated separately in the presence of  $H_2O_2$  (24 mM), urea (100 mM), or a combination  $H_2O_2$  (24 mM) + urea (100 mM). For all three cases, **Figure 2C** shows the horizontal fluid velocities in the region between the two pumps (x = 10mm) at different chamber depths, while holding *D* fixed at 1 mm. The flows in all three experiments exhibited positive velocities in the top half fluid layer (z > 0.8 mm), however, the system utilizing both substrates yielded a faster fluid velocity of 7.6  $\mu$ m/s at 75% of the chamber height, surpassing the fluid

velocities in the systems using single substrates (4.0  $\mu$ m /s for urea; 5.5  $\mu$ m /s for H<sub>2</sub>O<sub>2</sub>). Similarly, a fluid flow enhancement was observed at the bottom half layer (z < 0.8 mm), in the opposite direction.

We analyzed the flow rates between the two enzyme patches at different D, the separations between the patches. By comparing the fluid velocities created by different concentrations of substrates (**Figure S4**), a combination of 0.1 mM urea and 12 mM H<sub>2</sub>O<sub>2</sub> was used since they separately generate almost equivalent flows. For D values of 150, 300, and 800  $\mu$ m, the flow rates at the center between the two patches with mixed substrates were higher than those using single substrates (**Figure 2D**), with the flow rate reaching the fastest value (7.6  $\mu$ m/s) when D = 150  $\mu$ m. The synergistic effect of the two pumps ceases when D is increased to 1500 and 3000  $\mu$ m, which leads to flow rates lower when both substrates are present than that produced by the faster of the individual pumps (at 75% of the chamber height). Because of the presence of convective rolls, the horizontal flow velocities by single pump/substrate combinations also decreased with increasing distance (d) from the patch edge (**Figure S5**).

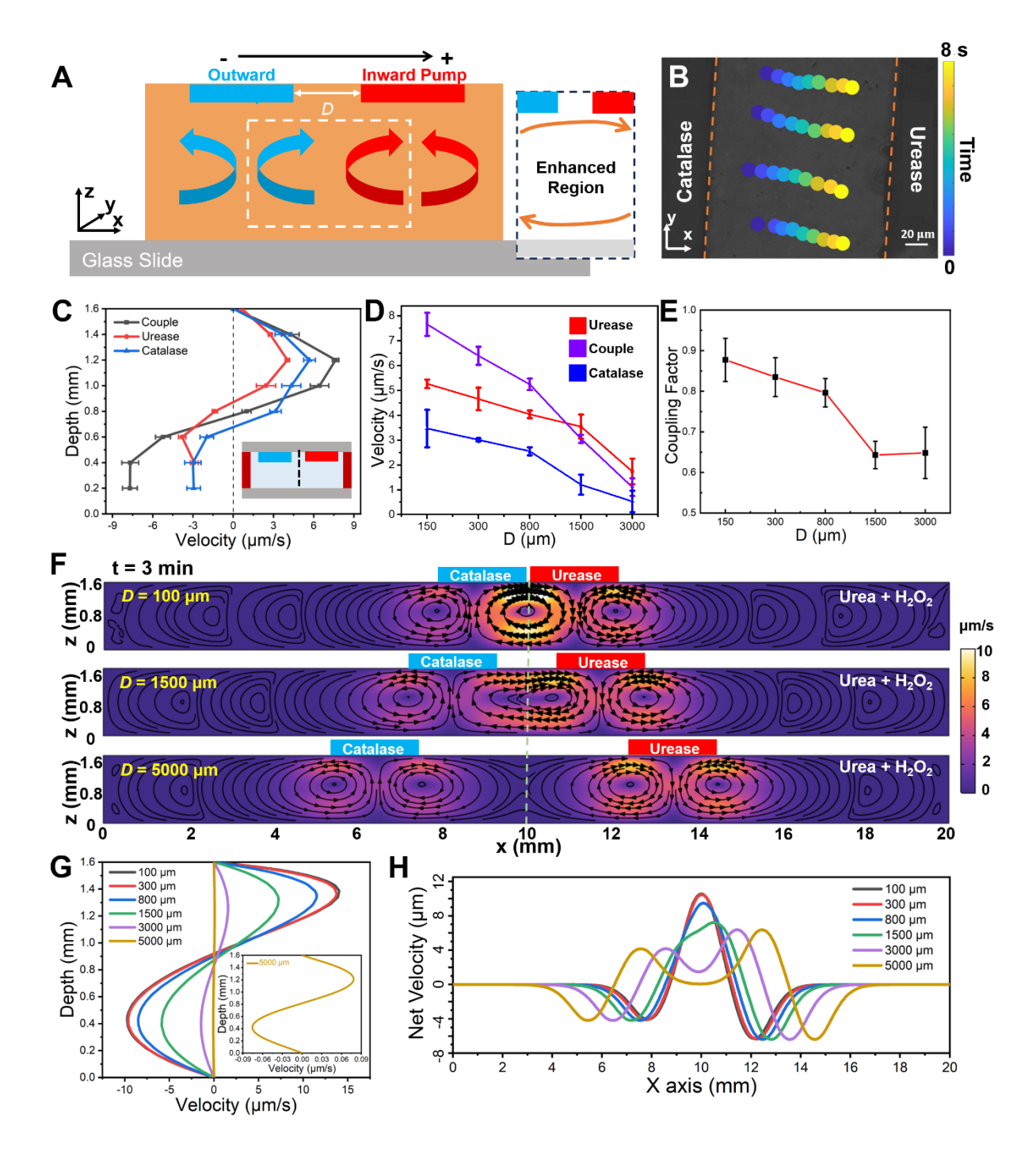


Figure 2. "Out" and "in" micropump-mediated enhancement of fluidic flow. (A) Schematic diagram of an "out-in" micropump system. Two patches coated by catalase and urease, respectively, were placed side by side separated by a distance D. The blue (catalase) and red (urease) arrows depict fluid flows by individual pumps, respectively. The inset shows the enhanced flow region with coupled pumping (orange arrows). (B) Real-time trajectories of tracers in urea/H2O2 mixture. See Video S1 for the movement of the tracers between two

patches. (C) The measured horizontal flow rates of urease pump (red curve), catalase pump (blue curve) and coupled pumps (black curve) at different depths of the chamber. D = 1 mm and d (distance from pump edge) = 0.5 mm. At 20x magnification, the depth of field is  $\sim$ 6  $\mu$ m. (D) The flow rates of coupled pumps with different D and individual pumps with different d (d = D/2) at 75% of the chamber height. (E) The coupling factor f versus D. (F) The simulated convective flows for urease/catalase pumps with different D (100, 1500, and 5000  $\mu$ m). The black arrows and streamlines show the fluid motion. The fluid velocity is quantified by the color bar. (G) The simulated horizontal velocity distribution with different D at x = 10 mm of the chamber and with varying z value. The inset focuses on the simulated S-curve for pumps with 5000  $\mu$ m distance. (H) Horizontal velocity distribution with different D at z = 1.2 mm of the chamber and with varying x value. The error bars representing standard errors are from three separate experiments and with 5 particles tracked in each experiment.

To quantify the effect caused by the separation D on the flows produced by the two pumps , we introduced a coupling factor  $(f = \frac{v_{coupled}(\frac{D}{2})}{v_{urease}(\frac{D}{2}) + v_{catalase}(\frac{D}{2})})$ . The parameter f measures the ratio between the flow rates at the center of the gap with both substrates present relative to the sum of individual pumping velocities with the respective single substrates in the same system. The value f = 1 indicates complete coupling of fluid flows from the two pumps, while decreasing f indicates less coupling. **Figure 2E** shows that the value of f decreases from 0.88 to 0.65 as D is increased from 150 to 3000  $\mu$ m.

To better visualize the system and understand the underlying mechanisms, we used computational modeling to investigate the coupling of catalase and urease micropumps. The values obtained from the simulations (**Figure 2F** and **Figure S6**) for the coupled convective flows at different D are consistent with the experimental observations. In the latter figures, the black arrows and streamlines represent the fluid direction. When the two pumps are close (D =

100  $\mu$ m), the vortex on the right from the catalase pump (see **Figure 1D**) coincides with the vortex on the left from the urease pump (**Figure 1C**) and the direction of flow in these two regions is the same. Hence, at the middle region (near x = 10 mm, top panel in **Figure 2F**), the combined flows effectively reinforce each other, leading to an increase in the flow rate; in this case,  $f \sim 0.9$ . As D is increased, the value of f decreases, leading to gradual attenuation of the coupled flow rates. At sufficiently large D, the two pumps operate independently. **Figure 2G** and **Figure 2H** show the simulation results for the horizontal velocity distribution at different D at x = 10 mm and at z = 1.2 mm of the chamber, respectively. The increase in flow rates in the middle region with decreasing D supports the proposed flow-enhancement mechanism.

## **Coupling of Two "In" Micropumps for Flow Cancellation**

While the above example led to additive effects, the two-pump system can also exhibit subtractive effects and cancellation of the flow. **Figure 3** shows an example of the latter scenario, involving two chemically identical micropumps; here, the two pumps involve urease. By itself, a single urease pump will produce inward flow. In **Figure 3A**, two such urease-coated pumps were placed side by side in a 0.1 M urea solution; the left urease patch constitutes Patch 1 (P1) and the right one constitutes Patch 2 (P2). Fluid flow from Patch 1 to Patch 2 (left to right) forms motion in the positive direction.

When the distance between two patches (D) was 1600 µm, the patches worked as two separate inward pumps (see schematic in **Figure 3A**). Namely, each individual patch subtends two convective rolls; the center of the two-roll configuration coincides with the center of the patch. **Figure 3B** shows that the flows at the left and right edges of P1 move in the opposite directions. (The flow at the left edge moves in positive direction, while the flow at the right edge moves in the negative direction.) Additionally, the magnitude of the flow rate about the right edge is roughly twice that at the left edge (which is affected by the flow from the neighboring patch).

Overall similar behavior is observed for P2. Note that the tracers in the middle spot (~800 μm from both patches) did not exhibit significant horizontal velocities (≈0 at the center).

Conversely, when the patches were placed close together (~300 µm apart), they worked cooperatively to behave as a single pump (**Figure 3C** and **Video S2**), where the fluid underneath each patch was propelled towards the center area (x = 10 mm). Here, both the left edge of P1 and fluid underneath P1 showed positive flow. Analogously, both the right edges of P2 and fluid underneath P2 displayed negative flow (**Figure 3D**). Again, the magnitude of the flow rate at the outer edges is greater than that at the neighboring inner edges and there was little horizontal velocity in the middle.

Based on the above observations (particularly the findings plotted in **Figure 3B**), we hypothesized that there should be an optimal separation between the patches that lies between the two extrema. At this optimal D, the flows from the two inner edges would move in the opposite direction (as in **Figure 3B**) but be sufficiently comparable in value as to effectively cancel each other and thus, yield a broad "no flow" zone in the central of the chamber (**Figure 3E**). The optimal D was found to be ~800  $\mu$ m. **Figure 3F** indicates the direction and magnitude of the flow rate at the different edges and the creation of a static fluid zone (see **Video S3** and corresponding simulations in **Figure 3I**).

Simulation results for the corresponding cases that involve two urease-coated patches are presented in **Figure 3G-I**. As observed in the experiments, the two pumps worked separately when they were far apart (**Figure 3G**), worked synergistically when they were close (**Figure 3H**). At the optimal  $D=800 \ \mu m$  (**Figure 3I**), a static zone was generated between the two inner edges of the micropumps, as seen from the tracer trajectories in **Figure 3J**. **Figure 3K** shows corresponding simulated fluid velocity  $u_z(x)$  ( $z=1.2 \ mm$ ) as a function of horizontal coordinate x. For an *intermediate* distance, the velocity remains low from  $x=9 \ mm$  to  $x=11 \ mm$ , correlating with the experimental observations (**Figure 3K**).

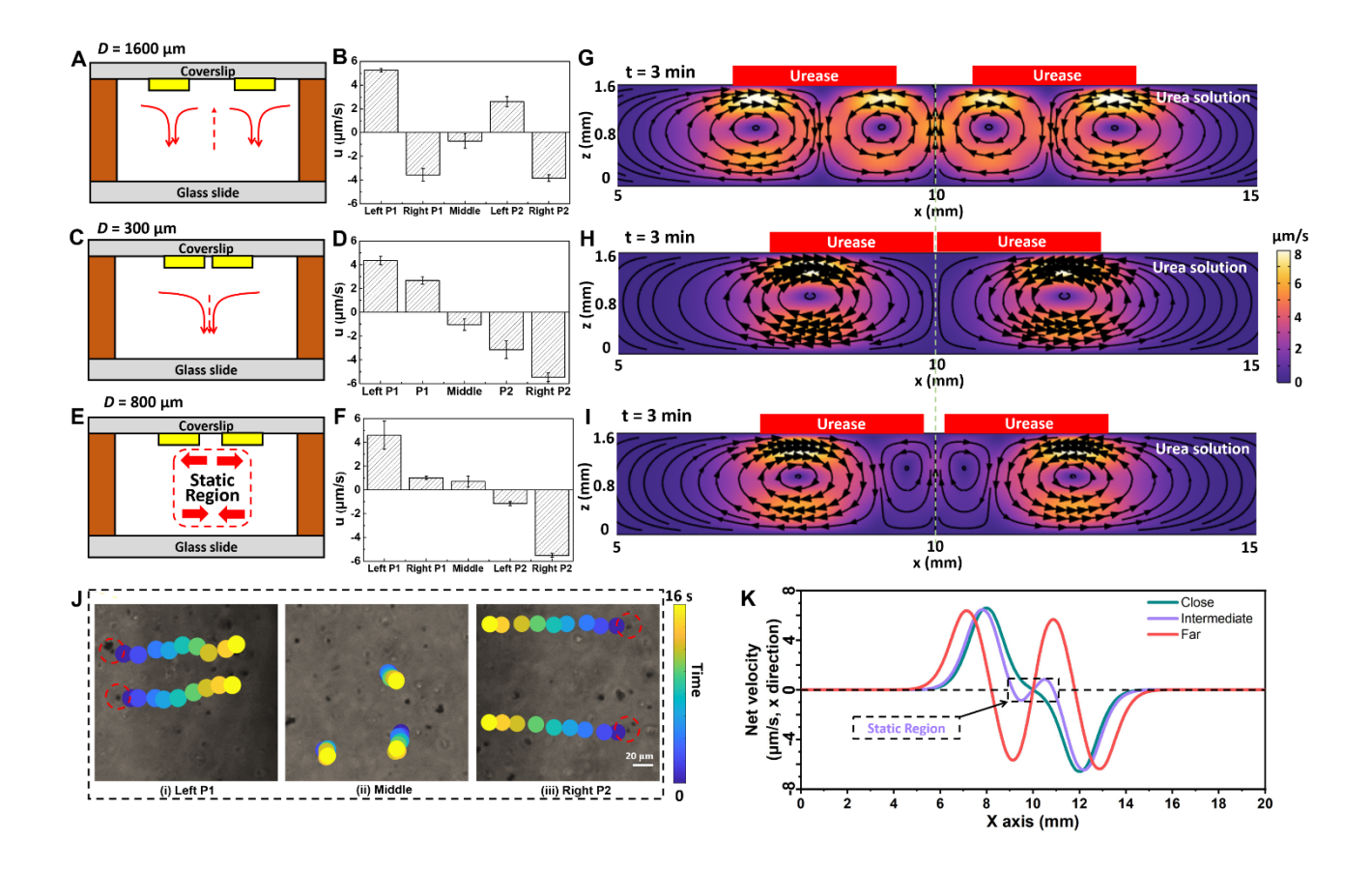


**Figure 3.** Two "in" micropump-mediated flow cancellation. The schematic diagram (A, C, E), the measured horizontal flow rates at different locations (B, D, F), and the simulated instantaneous convective flow dynamics (G, H, I) for two urease micropump system. Two patches were placed side by side with a different *D* of 1600 (A, B), 300 (C, D), and 800 μm (E, F), respectively. The red arrows in (A, C, E) represent the fluid directions underneath the patches. Corresponding far, close, and intermediate *D* values were selected for simulation in (G, H, I). The black arrows and streamlines represent the fluid direction. The fluid velocity is quantified by the color bar. Left P1 and right P1 mean left and right edges of Patch 1 (left patch in A, C, E), respectively; middle means at the center spot in the gap between the two patches; left P2 and right P2 mean left and right edges of Patch 2 (right patch in A, C, E), respectively; P1 and P2 mean spots directly underneath Patch 1 and Patch 2, respectively. See **Figure S7** for the corresponding scatter plots. (J) The trajectories of tracers flowing in a system with *D* = 800 μm. From left to right, they are tracers at (i) left edge of Patch 1, (ii) middle region and (iii) right edge of Patch 2. The scale

bar is 20  $\mu$ m. (K) The simulated horizontal velocity distribution with different *D* at the 3/4 height of the chamber (z = 1.2 mm).

# Coupling of Multiple Micropumps in 2-D Arrangement for Flow Enhancement and Deviation

Different combinations of urease and catalase pumps can create various fluid patterns in the system. Shown in **Figure S8**, four urease pumps were placed next to the edges of a catalase pump ( $D \sim 800 \ \mu m$ ). With the addition of both substrates in the solution, the velocities at all four edges were enhanced by ~2.5  $\mu m$ /s compared to a single catalase pump. This behavior is analogous to that seen in **Figure 2C**.

**Figure 4** shows a simple example of flow deviation: one catalase pump was placed at the bottom-right corner of the other catalase pump. The direction of the fluid flow expected for a single catalase pump was altered by the presence of the adjacent pump. The combined action of the two pumps resulted in a diagonal flow towards the top-right, as shown through both the simulation (white arrows in black dashed box, **Figure 4B**) and the experiments (deviated flow, **Figure 4C**). These designs further extend the concept of fluid flow regulation from aligned pumps (one dimension; 1D) to pump arrays (two dimensions; 2D).

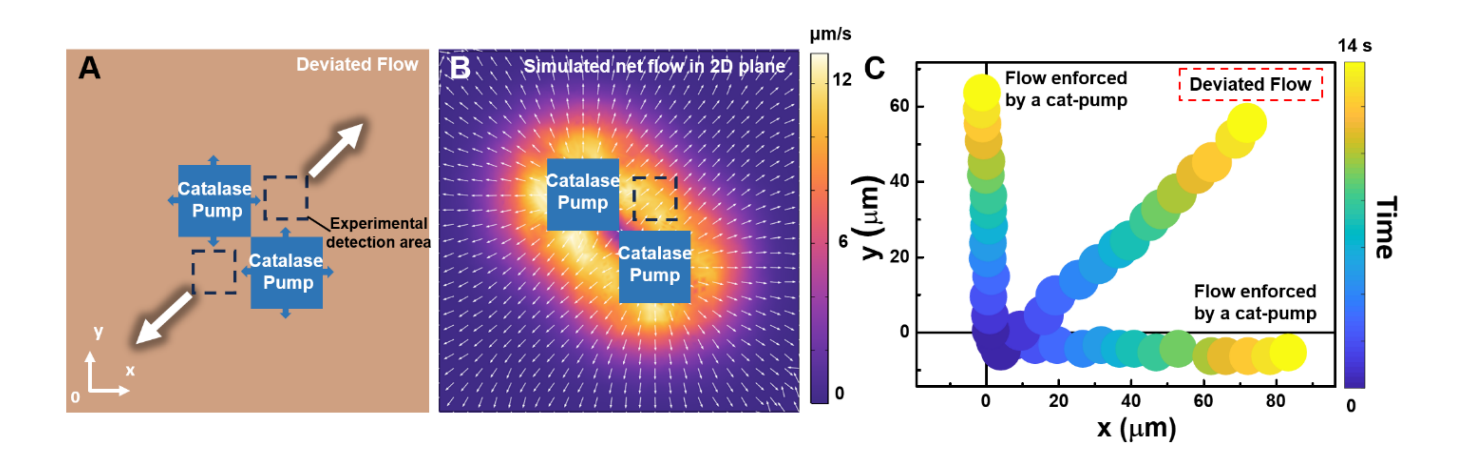


Figure 4. Control of the flow direction by 2D-arranged catalase pumps (see Figure S1B). (A) The top (2D) view of the experimental setup. (B) Simulation of fluid flow for a 2D-arranged catalase pump system. The white arrows represent the direction of the flow, while the color represents the simulated flow velocity. (C) Trajectories of tracers driven by individual catalase pumps (marked as Individual Catalase Pump) and catalase/catalase-coupled system (marked as Deviated Flow). The locations and speeds of the particles that follow the fluid flow were tracked using Tracker software, and then the trajectories of the individual tracers were plotted using Matlab.

#### Time-dependent Regulation of Fluid Flow in Enzyme Cascade Micropumps

As shown below, phosphatase, glucose oxidase and catalase constitute an enzyme cascade<sup>30</sup>:

Glucose 6 – phosphate 
$$\xrightarrow{Phosphatase} D - glucose + PO_4^{3-}$$
 (9)

$$D - glucose + H_2O + O_2 \xrightarrow{GOX} Gluconic acid + H_2O_2$$
 (10)

$$2H_2O_2 \xrightarrow{Catalase} 2H_2O + O_2 \tag{11}$$

Phosphatase converts glucose-6-phosphate to produce D-glucose; then glucose oxidase catalyzes the conversion of D-glucose to produce  $H_2O_2$ , which can be further decomposed by catalase. The motion of the tracers was first monitored in a GOx /catalase pump system (D = 1 mm) with 50 mM glucose as the substrates. (**Figure 5A and Video S4**). At t = 0, the GOx pump generates an outward flow, with the fluid near the top wall moving away from the pump (as in **Figure 1D**) whereas catalase pump is not triggered due to lack of its substrate. With time and the formation of  $H_2O_2$ , outward flow at the catalase pump kicks in, resulting in propulsion against the GOx pump (negative direction). In **Figure 5B**, the fluid at the center initially was flowing with a positive velocity, and it reversed its direction at ~85 seconds flowing towards GOx pump with

a negative velocity. The fluid in the phosphatase/GOx-coated pump combination also shows flow reversal in a 50 mM glucose 6-phosphate solution with the flow changing its direction at ~70 seconds. (**Figure S9**)

Simulation results for the time-dependent fluid flow in the micro-chamber are displayed in **Figure 5C-D**. Initially, streamlines were generated only under GOx pump since glucose was added as substrate (**Figure 5C**). With time, catalase pump was triggered and gradually dominated the propulsion of the fluid in the chamber. The intermediate in this cascade reaction is  $H_2O_2$ , and it requires a certain time period to transport (by diffusion and convection) from the GOx to the catalase patch. The  $H_2O_2$  concentration increases with time near the GOx patch, gradually diffuses to the surrounding area and is quickly consumed near the catalase patch (at x = 11 mm). The activation of the catalase pump then led to a time-dependent change in flow pattern, and flow reversal can be observed in the center region at x = 10 mm (**Figure 5D**). Specifically, at t = 4 min, GOx-pump dominated the flow in the chamber and an outward-pump was formed with positive velocity at x = 10 mm; whereas at t = 35 min, catalase-pump was mainly responsible for the flow, and a negative velocity was found at x = 10 mm. The peak growth at x = 7.5 mm indicates that the GOx-pump remains active through time. (**Figure 5D**)

We then placed AkP/GOx/catalase pumps in a row with D = 1 mm between each (**Figure S10**). Initially, only 50 mM glucose 6-phosphate was added in the micro-chamber, thus only AkP pump was triggered at t = 0, then the GOx and the catalase pumps would be activated sequentially. The red columns and blue columns represent the velocity at the middle between AkP/GOx and GOx/catalase pumps, respectively. The fluid flow changed direction at ~70 seconds in the gap between AkP/GOx patches, whereas for in the middle region between GOx/catalase pumps, it took them ~2 min to show reversed flow characterized by negative velocities. After both fluid reversals occurred, all three pumps still showed outward pumping at non-adjacent edges, indicating that these pumps were not inhibited (**Figure S10**).

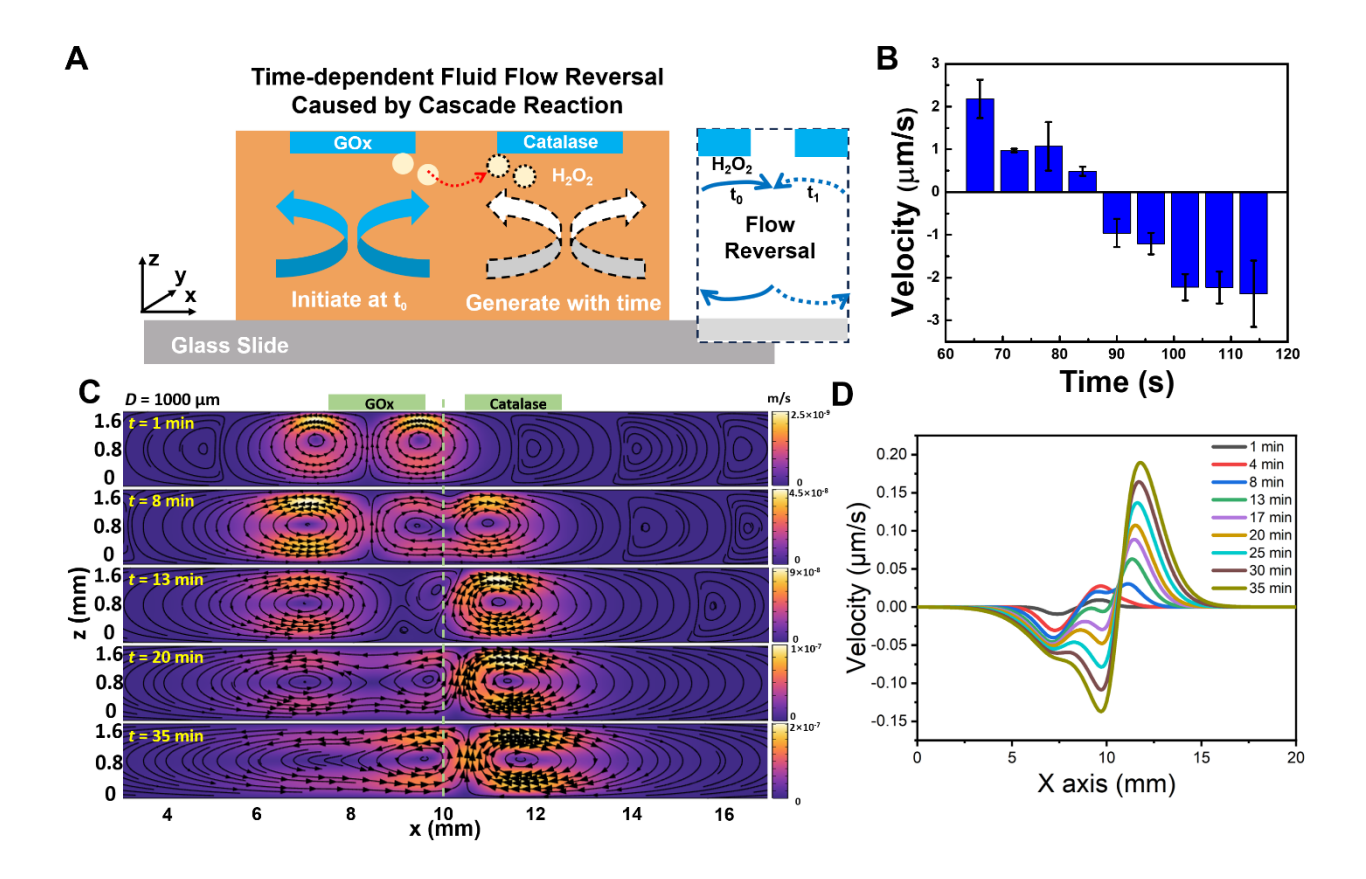


**Figure 5.** Time-dependent fluid flow reversal caused by cascade reaction. (A) Illustration of experimental setup for flow reversal based on a cascade reaction. GOx pump and catalase pumps were placed side by side with D = 1 mm. Initially, 50 mM glucose was added to the chamber to trigger GOx pump, and catalase pump kicked in with time due to the formation of H2O2 by GOx. Flow from left to right is defined as positive. The inset shows the flow reversal region (blue arrows). (B) Horizontal flow rate measured at the middle region of GOx/catalase pumps. Flow rate changing from positive to negative implies a switch from rightward to leftward direction in fluid flow. The error bars representing standard errors are from 3 separate experiments and with 5 particles tracked in each experiment. See **Figure S11** for the corresponding scatter plot. (C) The simulated instantaneous flow dynamics of cascade GOx/catalase pumps with a D of 1000 μm at different t (1, 8, 13, 20, and 30 min). The flow

reversal occurred within 13 min in simulation. (D) The simulated horizontal velocity distribution at different times at the 3/4 height of the chamber (z = 1.2 mm).

#### Multi-pump Systems as Vectorial Flow-based Multi-analyte Sensors

Based on the above results, we developed a system that can simultaneously evaluate real-time concentrations of multiple analytes. As shown in Figure 6A, we utilized urease and catalase pumps arranged perpendicularly to measure the concentrations of H<sub>2</sub>O<sub>2</sub> and urea in mixtures of the two. With the contributions from out-pumping catalase and in-pumping urease, the coupled system has an overall diagonal flow direction (purple arrow) moving from bottom right to top left in the region outlined by the dashed square. The fluid trajectories for the coupled pumps with different concentrations of added H<sub>2</sub>O<sub>2</sub> and urea were tracked (**Figure 6B**). With 0.1 M urea and 0 M H<sub>2</sub>O<sub>2</sub>, only the urease pump was activated, resulting in a flow along the y-axis. The addition of H<sub>2</sub>O<sub>2</sub> triggered the catalase pump, altering the flow direction (**Figure 6B**). This flow direction changed monotonically with increasing H<sub>2</sub>O<sub>2</sub> concentration and decreasing urea concentration until, with only 18 mM H<sub>2</sub>O<sub>2</sub> added, the flow was along the x-axis. The trajectory of the fluid flow determines the absolute concentrations of the analytes in the system. The magnitude and the direction of the fluid velocity vector are the outputs of the sensor and, with simple vector decomposition, the velocities V<sub>C</sub> and V<sub>U</sub> that represent the flow rates generated by the catalase pump and urease pump, respectively, can be determined. Standard calibration curves were generated correlating the flow rate with substrate concentration for both the urease pump (Figure S4B) and the catalase pump (Figure S4C). By plugging the V<sub>C</sub> and V<sub>U</sub> into the standard calibration curves, the absolute concentrations of each substrate in the mixture can be evaluated (Figure 6C). The readings obtained (as labeled on the y-axes of Figure 6C) from the sensor are close to the actual concentrations used in the system (as labeled on the x-axis). Notably,

most of the experimental concentrations are within the error bars of the readings from our enzyme-based sensors.

While we show the possibility of detecting hydrogen peroxide and urea only as a proof-of-concept, the precision of enzyme-pump-based biosensors can be improved by 1) generating more precise standard curves for the enzyme/substrate combinations, 2) measuring the direction and velocity of the fluid flow more accurately, and 3) increasing the chamber height and the patch size to increase the overall flow velocities.

Dynamic change of the flow direction in x-y plane can also be achieved by the positioning of the three-cascade reaction-based pumps as is indicated in **Figure 6D**. Initially, with 50 mM of glucose 6-phosphate, AkP pump produced an outward pumping flow which was toward GOx (Stage 1:  $V_x$ , ~0;  $V_y$ , negative); then the glucose oxidase started to pump, overpowering the fluid flow by the phosphatase (Stage 2:  $V_x$ , ~0;  $V_y$ , positive); finally, the flow created by the catalase pump coupled with the flow produced by GOx pump (Stage 3:  $V_x$ , positive;  $V_y$ , positive). At this stage, by comparing  $V_x$  to the standard curve in **Figure S4C**, the real-time local concentration of  $H_2O_2$  at the catalase pump can be determined (~6 mM  $H_2O_2$  near the catalase patch at Stage 3).

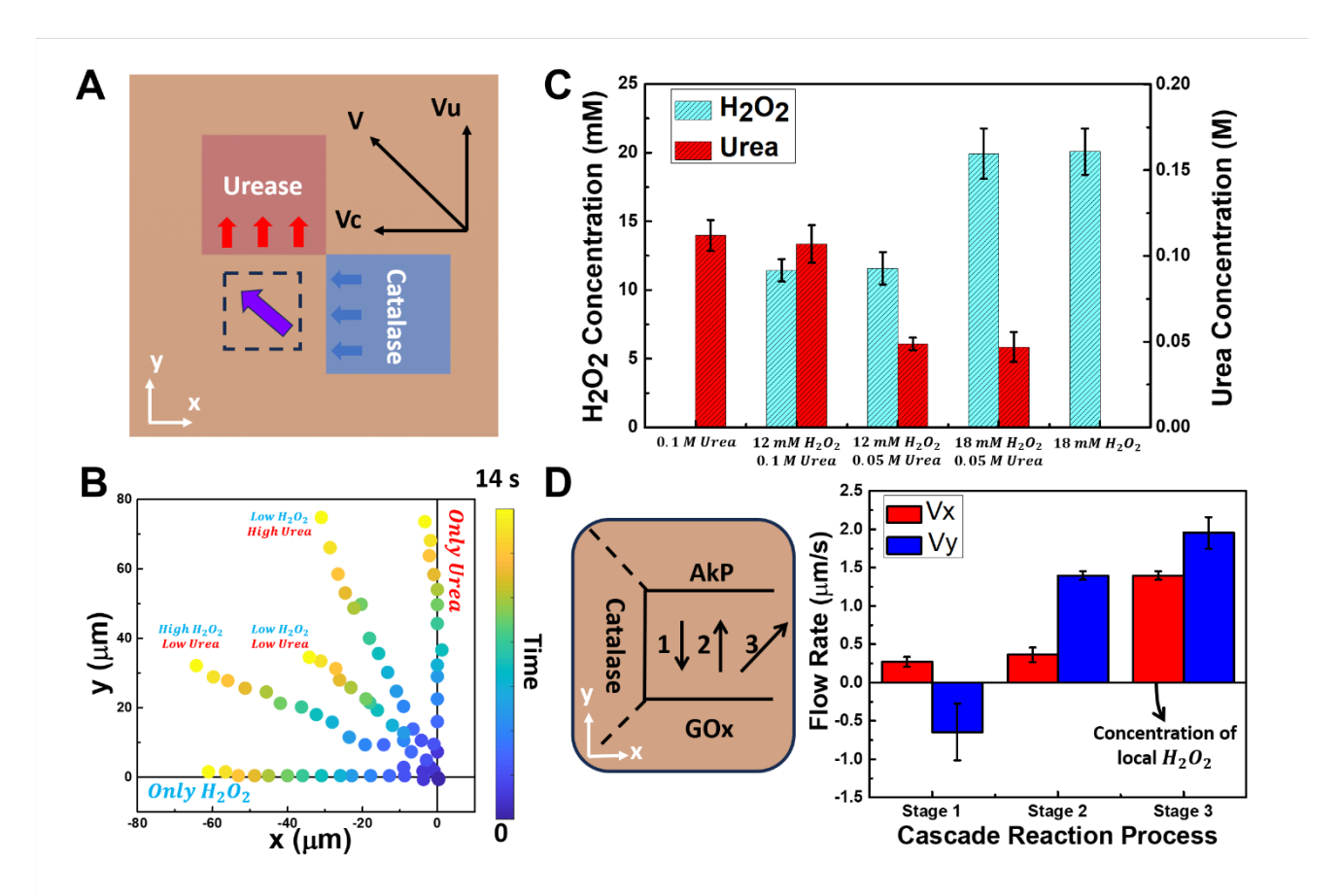


**Figure 6.** (A) Experimental setup of a urease-catalase multi-sensor in a micro-chamber. The urease was placed perpendicular to the catalase pump. The blue arrows and red arrows reveal the pumping direction of individual pumps, while the purple arrow reveals the fluid flows generated by the coupled system. (B) Trajectories of tracers under individual pumps and coupled pumps in 2D. Mixtures with different concentrations of  $H_2O_2$  and urea were added to the coupled system to test the sensing ability. The locations and speeds of the particles that follow the fluid flow were tracked using Tracker software, and then the trajectories of the individual tracers were plotted using Matlab. See **Video S5**. The results were obtained from 4 trials with 30 particles per trial. (C) Measured concentrations of mixed substrates in the multisensor system. X axis shows the actual concentrations of  $H_2O_2$ , and urea added, and the Y axes show the concentrations determined by the sensor. (D) 2D time-dependent fluid pattern

achieved using AkP-GOx-catalase cascade reaction in 2D. The arrows represent the flow direction that occur at Stage 1, Stage 2 and Stage 3. The graph shows the fluid velocities in at different stages. The Vx at Stage 3 can be used to monitor real-time local H<sub>2</sub>O<sub>2</sub> concentration during the cascade reaction. On the other hand, both the AkP- and GOx-pumps contribute to Vy, and therefore the individual concentrations of G6P and glucose cannot be obtained.

#### 4. Conclusion

Through a combination of experimental observations with numerical modelling, we analyzed capabilities of catalytic pumps to manipulate fluid flows. We used common catalytic reactions (which are controlled by well-known parameters) to design experimental setups that demonstrate such nontrivial behavior as flow enhancement, flow suppression, and changes in the directionality (reversal) of the fluid motion. The performed simulations suggest that the solutal buoyancy mechanism causes fluid motion and is responsible for all the observed effects. We found that combinations of the catalytic pumps represent a powerful tool that enables control over the speed and directionality of the fluid flows. Importantly, the speed and flow direction can be assigned independently by adjusting the appropriate concentration of reactants that activate the corresponding pumps. A fluidic system based on catalytic pumps that operate independently can be utilized as a versatile transportation system. 10,24 In particular, the addition of reactants with appropriate concentrations enables the delivery of the submerged cargo to different locations characterized by the orientation angle. Notably, the catalytic reactions are responsive only to specific reactants in the chemical mixtures. Therefore, the systems can operate as sensors that indicate concentrations of reactants through measurement of the trajectory along which the flow demonstrates maximal speed.

We also demonstrated the ability to dynamically control fluid flows through the cascade chemical reactions. Only a single reactant that activates the first pump in the cascade is required, which automatically entails subsequent reaction steps and associated changes in the flow speed and direction. The ability to change and even reverse the flow direction with time enables a delivery system that can transport the cargo to different locations at the prescribed time intervals. 10,24,27,31 Therefore, devices based on combinations of catalytic pumps enhance spatio-temporal control over microfluidic systems and provide new capabilities to manipulate cargo.

## Acknowledgement

The experimental work was supported by the National Science Foundation (CBET-2234134). The simulation work was supported by Hubei Key Laboratory of Biomass Fibers and Eco-dyeing & Finishing (STRZ202307).

#### ASSOCIATED CONTENT

## **Supporting Information**

Parameters Used in Simulation. Experimental setup of the pump system (Figure S1), immobilized-enzymatic activity measurement for urease, catalase and glucose oxidase (Figure S2), the simulated development of convective rolls that appear within the first 60 seconds (Figure S3), the measurements of the horizontal flow rate for individual enzyme pumps (Figure S4), the horizontal fluid velocity versus distance away from the patch edge (Figure S5), simulated out-in micropump systems with different D (Figure S6), the measured horizontal flow rates at different locations for two urease patches (Figure S7), two dimensional micropump array that enhances velocities of the fluid flow (Figure S8), time-dependent fluid flow reversal caused by AkP/GOx cascade reaction (Figure S9), time-dependent fluid flow reversal caused by AkP/GOx/Cat cascade reaction (Figure S10), horizontal flow rate measured at the middle region

of GOx/catalase pumps (Figure S11), parameters for the reagents used in the simulation (Table S1), enzyme parameters used in simulations (Table S2).

**Video S1**: Tracer motion in the region between a catalase patch (left) and a urease patch (right) with both substrates in the chamber (20x magnification)

**Video S2**: Tracer motion in the region between two urease patches close to each other (20x magnification)

**Video S3**: Tracer motion in the region between two urease patches separated by an intermediate distance (20x magnification)

**Video S4**: Tracer motion in the region between a glucose oxidase pump (bottom) and a catalase pump (top) with only glucose as the substrate (20x magnification)

**Video S5**: Diagonal motion of tracers produced by the perpendicularly arranged urease and catalase pumps with both urea and H<sub>2</sub>O<sub>2</sub> present in the solution (20x magnification)

#### Reference

- (1) Heinen, L.; Heuser, T.; Steinschulte, A.; Walther, A. Antagonistic Enzymes in a Biocatalytic pH Feedback System Program Autonomous DNA Hydrogel Life Cycles. *Nano Lett.* 2017, 17 (8), 4989– 4995. https://doi.org/10.1021/acs.nanolett.7b02165.
- (2) Chen, F.; Bai, M.; Cao, K.; Zhao, Y.; Cao, X.; Wei, J.; Wu, N.; Li, J.; Wang, L.; Fan, C.; Zhao, Y. Programming Enzyme-Initiated Autonomous DNAzyme Nanodevices in Living Cells. ACS Nano 2017, 11 (12), 11908–11914. https://doi.org/10.1021/acsnano.7b06728.
- (3) Hu, Y.; Sun, Y. Autonomous Motion of Immobilized Enzyme on Janus Particles Significantly Facilitates Enzymatic Reactions. *Biochemical Engineering Journal* 2019, 149, 107242. https://doi.org/10.1016/j.bej.2019.107242.
- (4) Zhao, X.; Gentile, K.; Mohajerani, F.; Sen, A. Powering Motion with Enzymes. *Acc. Chem. Res.* **2018**, *51* (10), 2373–2381. https://doi.org/10.1021/acs.accounts.8b00286.

- (5) Patiño, T.; Arqué, X.; Mestre, R.; Palacios, L.; Sánchez, S. Fundamental Aspects of Enzyme-Powered Micro- and Nanoswimmers. Acc. Chem. Res. 2018, 51 (11), 2662–2671. https://doi.org/10.1021/acs.accounts.8b00288.
- (6) Sun, J.; Mathesh, M.; Li, W.; Wilson, D. A. Enzyme-Powered Nanomotors with Controlled Size for Biomedical Applications. ACS Nano 2019, 13 (9), 10191–10200. https://doi.org/10.1021/acsnano.9b03358.
- (7) Sengupta, S.; Patra, D.; Ortiz-Rivera, I.; Agrawal, A.; Shklyaev, S.; Dey, K. K.; Córdova-Figueroa, U.; Mallouk, T. E.; Sen, A. Self-Powered Enzyme Micropumps. *Nature Chem* 2014, 6 (5), 415–422. https://doi.org/10.1038/nchem.1895.
- (8) Alarcón-Correa, M.; Günther, J.-P.; Troll, J.; Kadiri, V. M.; Bill, J.; Fischer, P.; Rothenstein, D. Self-Assembled Phage-Based Colloids for High Localized Enzymatic Activity. ACS Nano 2019, 13 (5), 5810–5815. https://doi.org/10.1021/acsnano.9b01408.
- (9) Zhou, C.; Zhang, H.; Li, Z.; Wang, W. Chemistry Pumps: A Review of Chemically Powered Micropumps. Lab Chip 2016, 16 (10), 1797–1811. https://doi.org/10.1039/C6LC00032K.
- (10) Das, S.; Shklyaev, O. E.; Altemose, A.; Shum, H.; Ortiz-Rivera, I.; Valdez, L.; Mallouk, T. E.; Balazs, A. C.; Sen, A. Harnessing Catalytic Pumps for Directional Delivery of Microparticles in Microchambers. *Nat Commun* 2017, 8 (1), 14384. https://doi.org/10.1038/ncomms14384.
- (11) Ortiz-Rivera, I.; Courtney, T. M.; Sen, A. Enzyme Micropump-Based Inhibitor Assays. *Advanced Functional Materials* **2016**, *26* (13), 2135–2142. https://doi.org/10.1002/adfm.201504619.
- (12) Gentile, K.; Maiti, S.; Brink, A.; Rallabandi, B.; Stone, H. A.; Sen, A. Silver-Based Self-Powered pH-Sensitive Pump and Sensor. *Langmuir* **2020**, 36 (27), 7948–7955. https://doi.org/10.1021/acs.langmuir.0c01240.
- (13) Parmar, J.; Vilela, D.; Villa, K.; Wang, J.; Sánchez, S. Micro- and Nanomotors as Active Environmental Microcleaners and Sensors. *J. Am. Chem. Soc.* **2018**, *140* (30), 9317–9331. https://doi.org/10.1021/jacs.8b05762.
- (14) Shukla, A. K.; Bhatia, D.; Dey, K. K. Convective Flow-Assisted Catalytic Propulsion of Polymer Beads Coated with Pd Nanoparticles for the Detection of Enzyme Inhibitors and Industrial Effluents. ACS Appl. Nano Mater. 2023, 6 (9), 8017–8027. https://doi.org/10.1021/acsanm.3c01333.

- (15) Alam, M.; Agashe, C.; Gill, A. K.; Varshney, R.; Tiwari, N.; Patra, D. Discrimination of Enantiomers and Constitutional Isomers by Self-Generated Macroscopic Fluid Flow. *Chem. Commun.* 2023, 59 (4), 434–437. https://doi.org/10.1039/D2CC05545G.
- (16) Gill, A. K.; Varshney, R.; Alam, M.; Agashe, C.; Patra, D. Maneuvering Fluid Motion and Flow-Induced Detection of Toxins by Enzyme Multilayer Films. ACS Appl. Bio Mater. 2021, 4 (8), 6203–6208. https://doi.org/10.1021/acsabm.1c00524.
- (17) Manna, R. K.; Gentile, K.; Shklyaev, O. E.; Sen, A.; Balazs, A. C. Self-Generated Convective Flows Enhance the Rates of Chemical Reactions. *Langmuir* 2022, 38 (4), 1432–1439. https://doi.org/10.1021/acs.langmuir.1c02593.
- (18) Ortiz-Rivera, I.; Shum, H.; Agrawal, A.; Sen, A.; Balazs, A. C. Convective Flow Reversal in Self-Powered Enzyme Micropumps. *PNAS* **2016**, *113* (10), 2585–2590. https://doi.org/10.1073/pnas.1517908113.
- (19) Song, J.; Shklyaev, O. E.; Sapre, A.; Balazs, A. C.; Sen, A. Self-Propelling Macroscale Sheets

  Powered by Enzyme Pumps. *Angewandte Chemie n/a* (n/a), e202311556.

  https://doi.org/10.1002/ange.202311556.
- (20) Gao, T.; McNeill, J. M.; Oliver, V. A.; Xiao, L.; Mallouk, T. E. Geometric and Scaling Effects in the Speed of Catalytic Enzyme Micropumps. *ACS Appl. Mater. Interfaces* **2022**, *14* (34), 39515–39523. https://doi.org/10.1021/acsami.2c09555.
- (21) He, H.; Lu, Y.; Qi, J.; Zhu, Q.; Chen, Z.; Wu, W. Adapting Liposomes for Oral Drug Delivery. *Acta Pharmaceutica Sinica B* **2019**, *9* (1), 36–48. https://doi.org/10.1016/j.apsb.2018.06.005.
- (22) Laskar, A.; Shklyaev, O. E.; Balazs, A. C. Designing Self-Propelled, Chemically Active Sheets: Wrappers, Flappers, and Creepers. *Science Advances* **2018**, *4* (12), eaav1745. https://doi.org/10.1126/sciadv.aav1745.
- (23) Laskar, A.; Manna, R. K.; Shklyaev, O. E.; Balazs, A. C. Computer Modeling Reveals Modalities to Actuate Mutable, Active Matter. *Nat Commun* **2022**, *13* (1), 2689. https://doi.org/10.1038/s41467-022-30445-x.
- (24) Maiti, S.; Shklyaev, O. E.; Balazs, A. C.; Sen, A. Self-Organization of Fluids in a Multienzymatic Pump System. *Langmuir* **2019**, *35* (10), 3724–3732. https://doi.org/10.1021/acs.langmuir.8b03607.

- (25) Jun, I.-K.; Hess, H. A Biomimetic, Self-Pumping Membrane. *Advanced Materials* **2010**, *22* (43), 4823–4825. https://doi.org/10.1002/adma.201001694.
- (26) Esplandiu, M. J.; Zhang, K.; Fraxedas, J.; Sepulveda, B.; Reguera, D. Unraveling the Operational Mechanisms of Chemically Propelled Motors with Micropumps. *Acc. Chem. Res.* **2018**, *51* (9), 1921–1930. https://doi.org/10.1021/acs.accounts.8b00241.
- (27) Shklyaev, O. E.; Shum, H.; Sen, A.; Balazs, A. C. Harnessing Surface-Bound Enzymatic Reactions to Organize Microcapsules in Solution. *Science Advances* 2016, 2 (3), e1501835. https://doi.org/10.1126/sciadv.1501835.
- (28) Valdez, L.; Shum, H.; Ortiz-Rivera, I.; C. Balazs, A.; Sen, A. Solutal and Thermal Buoyancy Effects in Self-Powered Phosphatase Micropumps. Soft Matter 2017, 13 (15), 2800–2807. https://doi.org/10.1039/C7SM00022G.
- (29) Gresho, P. M.; Sani, R. L. Incompressible Flow and the Finite Element Method. Volume 2: Incompressible Flow and Finite Element. Wiley, **1998**.
- (30) Gentile, K.; Bhide, A.; Kauffman, J.; Ghosh, S.; Maiti, S.; Adair, J.; Lee, T.-H.; Sen, A. Enzyme Aggregation and Fragmentation Induced by Catalysis Relevant Species. *Phys. Chem. Chem. Phys.* **2021**, *23* (36), 20709–20717. https://doi.org/10.1039/D1CP02966E.
- (31) Simó, C.; Serra-Casablancas, M.; Hortelao, A. C.; Di Carlo, V.; Guallar-Garrido, S.; Plaza-García, S.; Rabanal, R. M.; Ramos-Cabrer, P.; Yagüe, B.; Aguado, L.; Bardia, L.; Tosi, S.; Gómez-Vallejo, V.; Martín, A.; Patiño, T.; Julián, E.; Colombelli, J.; Llop, J.; Sánchez, S. Urease-Powered Nanobots for Radionuclide Bladder Cancer Therapy. *Nat. Nanotechnol.* 2024, 19 (4), 554–564. https://doi.org/10.1038/s41565-023-01577-y.

# **Table of Content**

